Imaging and Shape Analysis of GUVs as Model Plasma Membranes: Effect of *Trans* DOPC on Membrane Properties

Manasa V. Gudheti, Michael Mlodzianoski, and Samuel T. Hess
Department of Physics and Astronomy, University of Maine, Orono, Maine

ABSTRACT   Unsaturated *trans* fatty acids have been linked to a higher incidence of coronary artery disease, but not enough is known about the effect of *trans* lipids on membrane properties. Liquid-ordered (l_o) and liquid-disordered (l_d) membrane domains are implicated in various biological processes, such as endocytosis, adhesion, signaling, protein transport, apoptosis, and disease pathogenesis. The physical forces that induce domain formation and thus orchestrate cell function need to be further addressed and quantified. Here, we test the effect of *trans* DOPC (dielaidoyl phosphatidylcholine or DEPC) on the morphology of giant unilamellar vesicles (GUVs, used as a biomembrane model) made by electroformation with varying compositions of egg sphingomyelin, *trans* DOPC, *cis* DOPC, and cholesterol. GUVs were imaged by confocal fluorescence microscopy and then analyzed for changes in membrane morphology and properties such as l_o/l_d phase coexistence and area fractions, distribution of meridional curvature, and fluorescent-probe intensity distribution. BODIPY-FL-C_{12}-sphingomyelin, Lissamine rhodamine B dioleoylphosphatidylethanolamine and BODIPY-TR-C_{12}-sphingomyelin were used as fluorescent probes to differentially label the l_o and l_d phases. *Trans* DOPC induces some vesicles to form multidomain, invaginated morphologies that differ from the typical two-domain circular and truncated spherical shapes observed in its absence. *Trans* DOPC also alters the membrane curvature distribution; this is more pronounced in the l_o phase near the phase boundary, where significantly negative curvatures (<-0.5 μm^{-1}) are observed. A narrower distribution of meridional curvatures in GUVs with *trans* DOPC is suggestive of higher membrane bending rigidity. The ratio of average fluorescent intensities in the l_d/l_o phases indicates a greater concentration or brightness of the probes BODIPY-FL-C_{12}-sphingomyelin and BODIPY-TR-C_{12}-sphingomyelin in the l_o phase in the presence of *trans* DOPC. Addition of *trans* DOPC does not alter the l_o/l_d area fractions, indicating that it does not act like egg sphingomyelin, a saturated lipid. These changes in membrane properties seen in the presence of *trans* lipids could significantly impact cell function.

INTRODUCTION

Membrane heterogeneity is proposed to play a key role in important cell functions including lipid trafficking, signal transduction, immune system response, endo- and exocytosis, and disease pathogenesis (1–4). This heterogeneity in cell membranes arises due to the variety of lipid and protein species present and is, under some conditions, manifested by lateral phase separation of the membrane into liquid-ordered (l_o) and liquid-disordered (l_d) domains (5). The l_o domains, also referred to as lipid rafts (6), are enriched in cholesterol, saturated lipids such as sphingomyelin, GPI-anchored proteins, Src-family tyrosine kinases, palmitoylated and myristoylated proteins such as flotillins, and cholesterol-binding proteins such as caveolins (7). The l_o domains are more tightly packed (4,5) and exhibit higher bending rigidity (8) when compared to l_d domains, which are enriched in unsaturated phospholipids (7).

Rafts and raft proteins are associated with a multitude of diseases and have spurred intense research to understand the biophysical aspects of raft-mediated pathogenesis. For example, atherosclerosis, Parkinson's, Alzheimer's (9), and influenza (10) are some of the diseases to which rafts contribute. When compared to their *cis* counterparts, *trans* lipids

reduce activation of rhodopsin (a membrane receptor) in reconstituted membranes (11). In this contribution, we explore the effect of *trans* unsaturated lipids on domain formation and membrane shape distribution in model cell membranes, which may suggest mechanisms by which *trans* lipids could affect cell membranes and lead to abnormal physiology.

Trans fatty acids have been shown to increase the incidence of coronary artery disease and myocardial infarction (12) and to induce apoptosis in endothelial cells (13). Studies show that a 2% increase in energy intake from *trans* fatty acids is associated with a 25% increase in the risk of heart disease (14). It is estimated that *trans* fats make up 4–12% of the total dietary fat intake of the population in the United States (15). The amount of *trans* lipid that ends up in the membrane is reflective of *trans* lipid levels in the diet; the amount of *trans* fat incorporated into adipose tissue and red blood cells is related to food consumption (16–18). Although both *trans* fats and saturated fats increase low-density lipoprotein in blood, *trans* fats additionally decrease favorable high-density lipoprotein levels (12). *Trans* fats also inhibit the synthesis of beneficial polyunsaturated fatty acids and increase the influx of calcium into endothelial cells, which could induce stenosis (19,20). This evidence provides a strong rationale for studying the effects of *trans* lipids on biological membranes.

We investigate the effect of adding *trans* unsaturated lipid (in this case, dielaidoyl phosphatidylcholine or DEPC) to

membranes and study its effect on membrane properties such as curvature, l_o/l_d area fractions, and probe distribution using giant unilamellar vesicles (GUVs) as a biomembrane model. GUVs are advantageous model systems because of their ability to form curved bilayer structures with controllable composition while providing, under some conditions, phase-separated coexisting liquid domains large enough (>1 μm) to be resolvable by a light microscope (21–23). Small amounts ($\sim$1 part in 10^3) of fluorescent probes added to the lipids are used to visualize membrane domains using fluorescence confocal microscopy. We are using a ternary system consisting of egg sphingomyelin (ESM), *cis* unsaturated DOPC (*cis* DOPC or dioleoyl phosphatidylcholine), and cholesterol (CH) as the control system. We start with an equimolar ternary mixture of ESM, *cis* DOPC, and CH, which is known to phase-separate into coexisting liquid-ordered and liquid-disordered domains at room temperature (8,23–25), and then examine the effects of replacement of *cis* DOPC or ESM with *trans* DOPC (dielaidoyl phosphatidylcholine, or DEPC) (yielding a quaternary system). We chose DEPC (or *trans* DOPC) as the *trans* lipid for this study, since elaidic acid (the fatty acid component of DEPC) is the most abundant *trans* fat present in human atheromatous plaques (26).

The impact on membrane parameters of substituting some of the *cis* DOPC with *trans* DOPC is investigated using shape analysis. Shape-tracing analysis entails mathematically mapping the image of an equatorial section of a l_o/l_d phase-separated GUV and extracting the coordinates of the membrane as a function of arc length along the shape. We hypothesize that, due to its structural similarity to straight-chain saturated lipids, *trans* DOPC may behave more like sphingomyelin than *cis* DOPC, and we expect that it would preferentially distribute into the l_o phase. Finding probe combinations that can be used to distinguish l_o/l_d phases is critical for domain shape analysis. We used two probe combinations that exhibit differential partitioning between l_o and l_d domains: BODIPY-FL-C_{12}-sphingomyelin (BFL-Spm) and Lissamine rhodamine B DOPE (Rh-DOPE), and BFL-Spm and BODIPY-TR-C_{12}-sphingomyelin (BTR-Spm).

MATERIALS AND METHODS

Reagents, chemicals, and lipids

Chloroform, methanol, sucrose, HPLC-grade water, and sodium chloride (NaCl) were purchased from Fisher Scientific (Atlanta, GA). Dimethylsulfoxide and the antioxidant sodium-L-ascorbate were obtained from Sigma-Aldrich (St. Louis, MO). All chemicals and reagents were used without further purification and stored at room temperature. ESM, *cis* DOPC, *trans* DOPC (or DEPC), and CH were purchased from Avanti Polar Lipids (Alabaster, AL). The stock solutions of lipids were stored at $-20°$C to prevent oxidation and light-induced degradation.

Fluorescent probes

Rh-DOPE (ammonium salt) was purchased from Avanti Polar Lipids. BFL-Spm and BTR-Spm were obtained from Molecular Probes/Invitrogen (Eugene, OR), with BTR-Spm prepared by custom synthesis.

Preparation of giant unilamellar vesicles

Stock solutions of ESM, *cis* DOPC, *trans* DOPC, and CH were made in chloroform for a final concentration of 1 mM. Rh-DOPE was dissolved in methanol. BFL-Spm and BTR-Spm were dissolved in dimethylsulfoxide. The lipids were mixed in the desired ratios and the fluorescent probes were added to the mixture. The total mole percentage of fluorescent probes was always $\leq$0.6 mol %. Specifically, BFL-Spm, BTR-Spm, and Rh-DOPE constituted 0.078, 0.077, and 0.05 mol %, respectively, of the total lipid mixture, except when antioxidants were used, in which case BFL-Spm and Rh-DOPE were present at 0.5 and 0.1 mol %, respectively. Composition of GUVs are denoted in ratios of mole fractions of lipids as ESM/(*trans* DOPC, *cis* DOPC)/CH. The control sample is denoted as 1:(0,1):1, and a sample in which 20% of the *cis* DOPC is substituted by *trans* DOPC is denoted as 1:(0.2,0.8):1. The GUVs made with and without *trans* DOPC are denoted as *trans* GUVs and *cis* GUVs, respectively.

GUVs were made by electroformation (27,28). Two hundred microliters of the lipid mixture dissolved in chloroform was spread evenly on two indium tin oxide coated glass slides (Sigma-Aldrich) at 80°C. The slides were dried under vacuum for at least 2 h to remove the solvent. The slides were stacked on top of each other with the dried lipid layers facing each other and a Teflon spacer separating them. The space between the slides was filled with a solution (made with HPLC-grade water as the solvent), containing either 1), 100 mM sucrose; 2), 100 mM NaCl; or 3), 100 mM sucrose and 100 μM sodium ascorbate.

The slides were sealed with lithium grease (Panef, Milwaukee, WI) and connected to a function generator (3311A, Hewlett-Packard, Palo Alto, CA), producing an approximately sinusoidal wave with peak amplitude 2 V and frequency 10 Hz (measured using a Hewlett Packard 54503A digitizing oscilloscope) for 2 h. The electroformation procedure was carried out at 60°C to ensure uniform mixing of lipids. The GUVs obtained were stored in the dark at room temperature.

Confocal fluorescence microscopy

The GUVs were imaged using a Leica TCS-4D, TCS-NT, or TCS-SP microscope (Leica Microsystems, Exton, PA) at room temperature using an Olympus 60×/1.2 NA water, an Olympus 60×/1.35 NA oil, or a Leica 100×/1.4 NA oil objective. Axially symmetric equatorial vesicle sections to be used later for shape tracing were obtained. The laser lines used were 483 nm or 488 nm, and 543 nm or 568 nm. A FITC (RSP580, BP525/50)/TRITC (RSP650, LP 590) filter combination was used to do green-red dual channel imaging. BFL-Spm emits primarily in the green channel and Rh-DOPE and BTR-Spm emit in the red channel.

The pinhole size varied between 0.5 and 2 Airy units. The images were line- or frame-averaged 2–16 times. Typical voltage gains for the green channel and red channel were between 400 and 600 V, and 500 and 700 V, respectively, and the laser powers at the sample varied from $\sim$10 to 70 μW. Each objective was calibrated using a scale with known dimensions.

Shape tracing of equatorial confocal GUV slices

The least-squares algorithm written in MATLAB (version 7.0, The MathWorks, Natick, MA) is described in detail elsewhere (29). The basis of the algorithm is to use each pixel in the image as a data point, weighted by its uncertainty (estimated as the square root of the number of photons in that pixel), and then to fit a polynomial (typically of second order) through those data points. An RGB image of an equatorial section of a GUV of interest converted to a grayscale image is used for shape tracing. The pixel values of the images in the red and green channels are read from the RGB image. Some of the parameters that can be set are the width of the region being traced (typically 10–30 pixels), threshold (20–100), rotation angle (0°), step size (typically 1 or 2), and the length of the trace (depends on the size of the vesicle to be traced). For a GUV of $\sim$20 μm size, $\sim$400–500 points represent one complete trace. The initial x and y trace positions are chosen

manually to ensure that the tracing commences at a point on the vesicle itself. A rectangular region centered on the trace position, set by the width of the trace, is fit using a second-order polynomial. The threshold determines the minimum brightness that a pixel should have within this rectangular box to be considered for the polynomial fit (of the form $y = \alpha x^2 + \beta x + \gamma$), where locally y points perpendicular to the vesicle trace toward larger radius, and α, β, and γ are free parameters. The fit is then used to calculate the meridional curvature (-2α) and the direction of the next step and subsequent trace position based on the step size. The tracing algorithm outputs the following information: x and y coordinates; membrane path angle (ψ) within the equatorial plane, measured relative to the horizontal axis; meridional curvature (C_m); and pixel intensities in the red and green channels as a function of arc length (S). $C_m = 1/R = d\psi/dS$, where R is the radius of a circle tangent to the path at the point of interest. From our calculations, we are able to obtain curvature values with an uncertainty of $\sim \pm 0.001 \ \mu m^{-1}$.

Shape traces are rotated to align the shape to be symmetric with the y axis, and each of the two sides of the symmetric shape is analyzed individually to obtain l_o and l_d area fractions, meridional curvatures, probe partitioning behavior, and location of the phase boundary. For each equatorial vesicle section, all the parameters are obtained as a function of arc length for each symmetric side individually. Nineteen *trans* GUVs and 18 *cis* GUVs were analyzed with this method.

Determination of phase boundary between l_o an l_d domains

The l_o and l_d phases were labeled using fluorescent lipid analogs and visualized by confocal microscopy. Rh-DOPE, which contains unsaturated acyl chains, is expected to be excluded from the ordered phase, and in previous studies has been used as a l_d phase marker (30,31). Since Rh-DOPE is detected primarily in the red channel, plotting the red pixel intensity as a function of arc length gave us the edge of the l_d phase and, consequently, the location of the phase boundary. BFL-Spm partitions into both phases and is detected primarily in the green channel. Hence, the l_d phase appears yellow/orange in the two-color merged image. It is harder to determine the phase boundary when the BFL-Spm/ BTR-Spm probe combination is used, since both probes partition into both phases. In this case, too, there is a difference in probe partitioning between the domains, and by plotting the red and green pixel intensities as a function of arc length, the phase boundary can be determined. When it was not possible to identify the phase boundary using the probe partitioning profile (8 out of 37 GUVs traced, occurring only with the BFL-Spm/BTR-Spm probe combination), image processing software was used to manually identify the phase boundary. This is done for both sides of the vesicle separately.

Determination of area fractions

Each side of the symmetric equatorial section is analyzed separately. The equations listed below are used for computing the area fractions. The differential arc length (Δs_i) for the ith step is determined using $\Delta s_i = \sqrt{((\Delta x_i)^2 + (\Delta y_i)^2)}$, where Δx_i and Δy_i are the displacements in radial x and axial y coordinates, respectively. Then the differential area (ΔA_i) for the ith step in the trace is computed using $\Delta A_i = 2\pi x_i \Delta s_i$, and summed over the entire surface to yield the total area $A_t = \sum \Delta A_i$. The area of phase 1 (A_1) is calculated by summing up to the phase boundary, and the area of phase 2 (A_2) is obtained from $A_2 = A_t - A_1$, namely the difference between the total area A_t and the area of the first phase A_1, where $A_1 = \sum_0^b \Delta A_i$, where b is the location of the phase boundary. If A_1 is denoted as the l_d area and A_2 as the l_o area, the l_d area fraction is A_1/A_t and the l_o area fraction is A_2/A_t. This was done for 36 GUVs, 18 with *trans* DOPC and 18 without.

Histograms of curvatures

Meridional curvatures of axially symmetric equatorial sections of GUVs were obtained from the shape-tracing algorithm. We selectively chose two-domain unilamellar GUVs with comparable sizes when building the histograms. We analyzed 18 *cis* GUVs and 19 *trans* GUVs. Histograms of curvatures observed at each pixel in the image of the entire equatorial section of the vesicle (overall), near the phase boundary, in the l_o and l_d phases, and near the l_o and l_d phase boundary were compiled separately using a MATLAB routine. To determine the curvatures near the phase boundary, points encompassing $\pm 1 \ \mu m$ on either side of the phase boundary were selected. The number of points (n) and bins used for plotting the histograms are listed in Table 1. The histogram bins were linearly spaced between -0.9 and $+0.6 \ \mu m^{-1}$.

Determination of the mean and second moment of meridional curvature distribution

The mean meridional curvature $\langle C_m \rangle$ for each curvature histogram is computed using

$$\langle C_m \rangle = \frac{\sum_i N_i C_m^{(i)}}{\sum_i N_i}, \tag{1}$$

where N_i is the number of points in the histogram that have $C_m^{(i)}$ as the curvature value. From the same curvature histograms, the second moment S is calculated using

$$S = \frac{\sum_i N_i (C_m^{(i)} - \langle C_m \rangle)^2}{\sum_i N_i}, \tag{2}$$

The second moment, which is the variance, is computed as a measure of width of the curvature distribution.

Quantification of intensity ratios of fluorescent lipid analogs in GUV equatorial sections

From shape analysis of the equatorial GUV sections, we obtain fluorescent probe intensity as a function of arc length for each symmetric side. The average fluorescence intensity of each probe in the l_o and l_d phase is determined for each side of the vesicle by using the entire trace on that side. The ratio of the fluorescence intensities in l_d and l_o phases, referred to as the intensity ratio, is computed for each symmetric side. The average intensity ratio for each vesicle is obtained by taking the average of the two sides. The intensity of a fluorescent probe in a particular phase is proportional to the product of the concentration of the probe and the brightness of the probe in that phase. The brightness of the probe (equal to the product of the fluorescent probe's molar absorption coefficient and the quantum yield) is in turn influenced by the environment surrounding the probe.

RESULTS

The effect of *trans* lipids on membrane properties is divided into two categories: 1), three-dimensional structural effects

TABLE 1 Numbers of points (*n*) and bins used for plotting histograms of meridional curvatures

Type of GUVs (*N*)	Overall	Phase boundary	l_o	l_d	l_o Phase boundary	l_d Phase boundary
cis GUVs (18)	6846	497	3752	3130	249	285
trans GUVs (19)	7345	533	3880	3503	283	288
Number of bins	100	25	75	75	15	15

The bins were linearly spaced from -0.9 to $+0.6 \ \mu m^{-1}$. Number (*N*) of GUVs analyzed were 18 *cis* and 19 *trans* GUVs. l_o, liquid-ordered; l_d, liquid-disordered.

that are manifested as changes in GUV morphology, the presence of invaginations, and alterations in meridional curvature distributions; and 2), two-dimensional lateral effects that are characterized by the presence of multiple domains, l_o/l_d area fractions, and fluorescent probe distributions.

Morphology of GUVs is dependent on composition

Vesicle composition strongly influences the shape of GUVs obtained (see Fig. 1) with mixtures of egg sphingomyelin, DOPC, and cholesterol. The panels show two-channel merged images exhibiting two-phase (l_o/l_d) fluid-fluid coexistence. While the red channel emission primarily contains fluorescence from either Rh-DOPE or BTR-Spm in the l_d phase, the green emission channel contains fluorescence from the BFL-Spm probe in both the l_o (*green regions*) and l_d

(*yellow/orange regions*) phases. Because Rh-DOPE has been shown previously to partition primarily into the l_d phase (30,31) and because it was excluded from the phase which also had smaller observed conformational fluctuations and undulations (data not shown), the phase containing Rh-DOPE was determined to be the l_d phase (*yellow/orange membrane regions*). The phase boundary is clearly discernible in all the panels. In Fig. 1, *A–D* and *I–L* are images of a control sample with ESM/(*trans* DOPC, *cis* DOPC)/cholesterol ratios of 1:(0,1):1, and they show the typical circular and truncated spherical shapes obtained in the presence of *cis* unsaturated lipids. Phase coexistence, line tension, and some of the same types of shapes, including truncated spheres, are observed in NaCl solution (Fig. 1, *I* and *J*), but the yield is considerably lower ($\sim$14% of that obtained in sucrose). The existence of line tension in the images is confirmed by the presence of separate phases with rounded boundaries; in
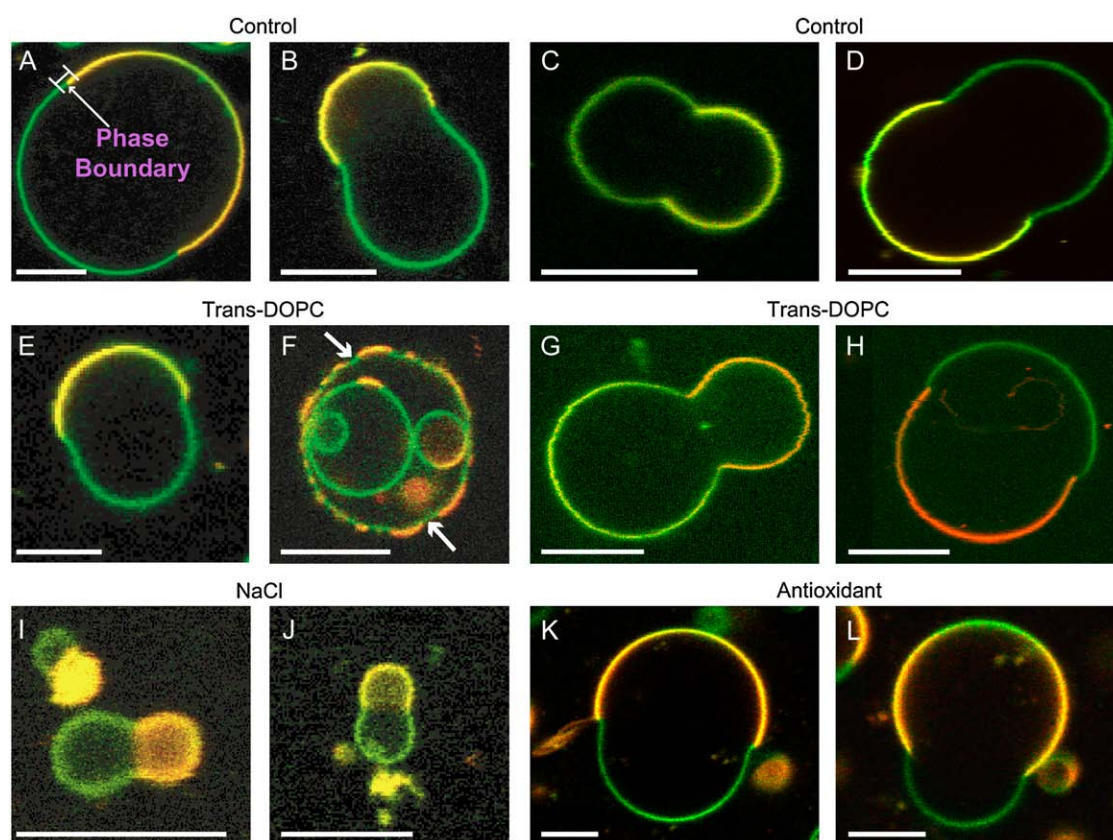

FIGURE 1 Fluorescence confocal microscopy images showing equatorial sections of giant unilamellar vesicles (GUVs) with fluid-fluid l_o/l_d phase coexistence. The fluorescent probes used were BFL-Spm and Rh-DOPE, except in *C* and *G*, where BFL-Spm and BTR-Spm were used. Images superimpose red (Rh-DOPE or BTR-Spm emission) and green (BFL-Spm emission) channels. The green regions of the GUVs are identified as the l_o phase and the yellow/orange membrane regions are identified as the l_d phase (see text). Scale bars, 10 μm. Images were obtained at room temperature. The composition of the GUVs is denoted by the ESM/(*trans* DOPC, *cis* DOPC)/CH ratios: 1:(0,1):1 (*A–D* and *I–L*); 1:(0.2,0.8):1 (*E*, *G*, and *H*), and 1:(0.5,0.5):1 (*F*). GUVs were made using 100 mM sucrose (*A–H*), 100 mM NaCl (*I* and *J*), and 100 mM sucrose + 100 μM sodium ascorbate (*K* and *L*) as the electroformation solutions. Notice that GUVs containing *trans* DOPC (*E* and *F*) show a pronounced negative (bending inward) curvature; this is especially pronounced in the l_o (*green*) phase in *F*, where a large number of invaginations (*arrows*) are observed. GUVs made in NaCl (*I* and *J*) were smaller than those made in sucrose. The arrow in *A* points to the phase boundary and the line represents the typical region considered for compiling the histograms of meridional curvatures near the phase boundary ($\sim$±1 μm on either side of the phase boundary). (*C*, *D*, *G*, and *H*) Examples of two-domain GUVs that were used to compile the curvature histograms.

the absence of line tension, domains would not minimize their boundary perimeter, or a single phase would be present. Small line tension values allow nearly spherical vesicles to minimize the total energy, whereas in the presence of significant line tension, domains frequently form truncated spheres joined at the phase boundary with a significant contact angle. Fig. 1, *E*, *G*, and *H*, with lipid ratios of 1:(0.2,0.8):1, and Fig. 1 *F*, with lipid ratios of 1:(0.5,0.5):1, show samples of shapes obtained when *trans* DOPC is present. Truncated and spherical shapes are commonly observed in the presence of *trans* DOPC along with some unusual shapes as observed in Fig. 1 *F*. Fig. 1, *C*, *D*, *G*, and *H*, show examples of GUVs that are used to compile the curvature histograms; notice that they are all vesicles with two domains, as we do not use multidomain (more than two-domain) vesicles (Fig. 1 *F*) in the shape-tracing analysis. Also note the negative meridional curvature (bending inward) in the l_o phase (Fig. 1 *F*, *arrows*).

Lipid peroxides, which can be formed by photochemical reactions in the presence of fluorescent dyes, can lead to phase separation in GUVs composed of lipid mixtures that would not otherwise phase separate (32). It has been proposed that the presence of antioxidants prevents phase separation induced by lipid peroxidation (32). Fig. 1, *K* and *L*, show GUVs (1:(0,1):1) made in the presence of 100 μM sodium ascorbate, a concentration that is physiologically relevant (33). The GUV shapes obtained in the presence of antioxidants are similar to those obtained in its absence, despite the fact that a higher concentration of fluorescent dyes was used in the lipid mixture when making GUVs in the antioxidant solution.

Presence of *trans* DOPC induces unusual GUV shapes

Fig. 2 shows a variety of GUV shapes that are obtained in the presence of *trans* DOPC. It shows compositions 1:(0.2,0.8):1 (*A* and *B*) and 1:(0.5,0.5):1 (*C* and *D*). Fig. 1, *E* and *F*, shows GUVs that have a fraction of sphingomyelin substituted with *trans* DOPC, the composition being 0.8:(0.2,1):1. Fig. 1, *G* and *H*, shows GUVs containing *trans* DOPC but no *cis* DOPC, with the composition 1:(1,0):1. In the absence of *trans* DOPC, circular and truncated spheres are typically observed (as seen in Fig. 1), although on occasion we do observe shapes that deviate from the typical morphology. The addition of *trans* DOPC enhances the formation of "unusual" shapes (nonaxiosymmetric shapes), including those shown in Fig. 2. To quantify relative probabilities of these shapes, we tabulated their incidences: we find 35% are unusual shapes in *trans* GUVs ($n = 40$), as opposed to only 10% in *cis* GUVs ($n = 40$). Also evident in Fig. 2 (*arrows*) are areas of negative curvature in the l_o (*green*) phase. Small invaginations in the l_o phase are observed when *trans* DOPC is present. These invaginations have large negative meridional curvature (< -0.5 μm^{-1}), where the l_o (*green*) phase bends inward toward the center of the shape (e.g., see Fig. 1 *F*).
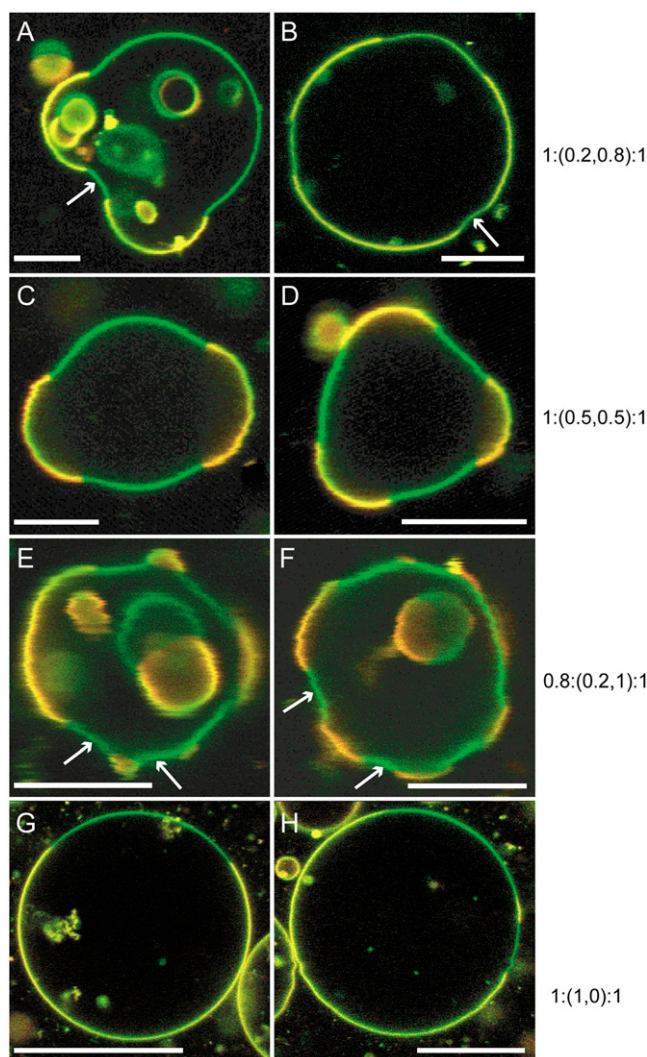

FIGURE 2 Presence of *trans* DOPC induces unusual GUV shapes. Equatorial sections of *trans* GUVs were imaged at room temperature. Scale bars, 10 μm. The BFL-Spm (*green channel*)/Rh-DOPE (*red channel*) fluorescent probe combination was used in all panels except *B*, where the probes used were BFL-Spm (*green channel*)/BTR-Spm (*red channel*). The green and yellow/orange regions correspond to l_o and l_d phases, respectively. The GUV compositions (ESM/(*trans* DOPC, *cis* DOPC)/CH) are as follows: (*A* and *B*) 1:(0.2,0.8):1; (*C* and *D*) 1:(0.5,0.5):1; (*E* and *F*) 0.8:(0.2,1):1; and (*G* and *H*) 1:(1,0):1. Note that all the images in *A–F* have multiple (more than two) domains. When 80 images containing *trans* DOPC were analyzed for the presence of multiple domains, it was found that 42 of them had multiple domains. Many GUVS have inward curvature in the l_o (*green*) phase (*arrows*). The solution used for electroformation was 100 mM sucrose.

Significant differences in the distribution of meridional curvatures in GUVs made with and without *trans* DOPC

Histograms of meridional curvatures are plotted for 18 *cis* GUVs and 19 *trans* axiosymmetric GUVs. Table 1 lists the parameters used for obtaining the curvature histograms. Overall curvatures, curvatures at the phase boundary, curvatures in the

l_o and l_d domains, and curvatures in the l_o and l_d phases near the phase boundary are plotted separately (Figs. 3–6). Table 1 lists the number of points and bins used to plot the histograms and Table 2 lists the percentage of positive and negative meridional curvature values for each histogram and the corresponding figure number (listed in the first row), as well as the mean curvature value and second moment of the curvature histogram. The mean curvature and second moment are calculated using Eqs. 1 and 2, respectively.

Fig. 3 shows the histograms of overall meridional curvatures (along the surface of the entire equatorial vesicle section) for *cis* and *trans* GUVs. Significantly negative curvatures are
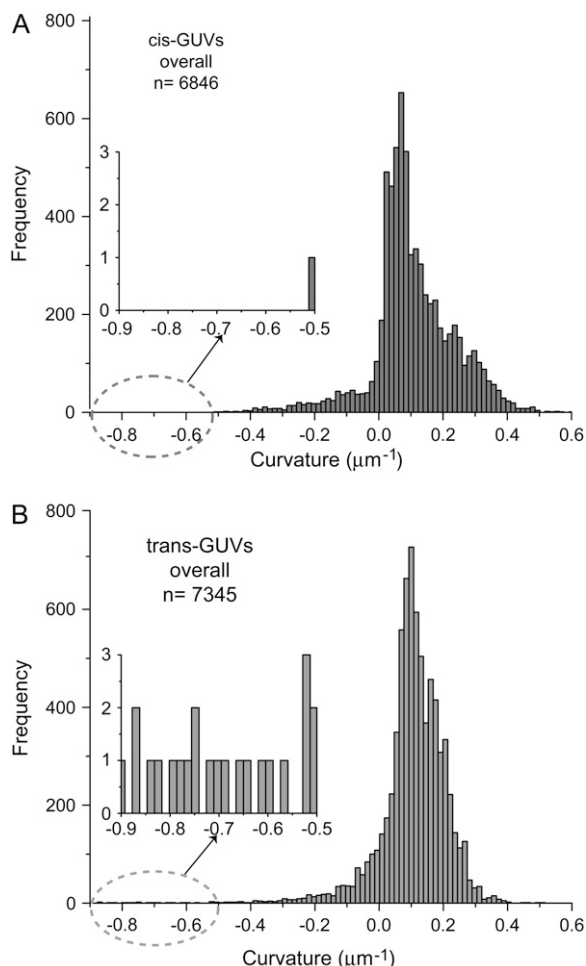

FIGURE 3 Significant difference in the distribution of overall meridional curvatures between *cis* and *trans* GUVs. Histograms of curvatures (using 100 bins) were compiled using a MATLAB tracing program. The *cis* GUVs exhibit a wider distribution, as characterized by the second moment ($S = 0.016 \pm 0.001 \ \mu m^{-2}$ for *cis* GUVs and $S = 0.012 \pm 0.001 \ \mu m^{-2}$ for *trans* GUVs), which is suggestive of lower bending rigidity than in *trans* GUVs. Despite the difference in the curvature distributions, the mean is similar: $\langle C_m \rangle = 0.106 \pm 0.002 \ \mu m^{-1}$ for *cis* GUVs and $\langle C_m \rangle = 0.105 \pm 0.002 \ \mu m^{-1}$ for *trans* GUVs. (*Insets*) Expanded views of overall curvatures in the -0.9 to $-0.5 \ \mu m^{-1}$ range; significantly negative curvatures ($< -0.5 \ \mu m^{-1}$) possibly represent invaginations present in *trans* GUVs that are absent in *cis* GUVs. The number of points, *n*, is 6846 and 7345 for *cis* and *trans* GUVs, respectively.

present in the *trans* GUVs (Fig. 3 *insets*). It is interesting to note that, despite the fact that both the histograms have the same fraction of negative curvature values (10%), the distributions are significantly different. The width of the distribution is greater in *cis* GUVs (Fig. 3 *A*) when compared to *trans* GUVs (Fig. 3 *B*), as revealed by the second moment (Table 2, *bottom row*). Despite the differences, the mean of both distributions is similar (Table 2, *fourth row*).

Fig. 4 shows the histograms of meridional curvatures for *cis* and *trans* GUVs near the phase boundary. The curvature distribution in *trans* GUVs (Fig. 4 *B*) is skewed toward negative curvature values. The *cis* and *trans* GUVs have a similar fraction of negative curvature values at the phase boundary (74% vs. 72%). Despite the similarities in the distributions, the mean curvature is more negative for *cis* GUVs compared with *trans* GUVs (Table 2, *fourth row*). The features in *trans* GUVs with strongly negative meridional curvatures ($< -0.5 \ \mu m^{-1}$) are possibly reflective of small invaginations. The *cis* GUVs imaged did not have these features. Most ($\sim$75%) of the invaginations in the *trans* GUVs are present within $\pm 1 \ \mu m$ of the phase boundary.

Pronounced negative curvature found in l_o phase near phase boundary of *trans* GUVs

Fig. 5 shows the meridional curvature distribution in the l_o and l_d phases, and Fig. 6 shows the distribution of meridional curvatures near the individual (l_o and l_d) phase boundaries. The width of the curvature distribution for *cis* and *trans* GUVs is similar (Fig. 5, *A* and *B*) in the l_o phase, as determined by the second moment values (Table 2, *bottom row*), but the histograms are different in the l_d phase in the presence and absence of *trans* lipids (Fig. 5, *C* and *D*, and Table 2, *bottom row*). The mean curvature values are similar in the l_o and l_d phases for *cis* GUVs (Fig. 5, *A* and *C*, and Table 2, *fourth row*), whereas for *trans* GUVs the mean curvature is lower in the l_o phase than in the l_d phase (Fig. 5, *B* and *D*, and Table 2, *fourth row*).

The l_o phase boundary curvature distribution for *trans* GUVs is also skewed more toward negative values than it is for *cis* GUVs (Fig. 6, *A* and *B*). Although the mean meridional curvature values near the l_o phase boundary are similar (Table 2, *fourth row*), compared with *cis* GUVs (Fig. 6 *A*, and Table 2, *third row*), *trans* GUVs (Fig. 6 *B*) show a slightly larger fraction of curvatures that are negative. Moreover, *trans* GUVs have a greater fraction of curvatures to the left of the peak (34% for *trans* vs. 24% for *cis*) in the l_o phase near the phase boundary (Fig. 6, *A* and *B*).

Greater number of vesicles with multiple domains observed in the presence of *trans* DOPC

One feature common in Fig. 2, *A–F*, is the presence of *trans* DOPC and multiple (more than two) domains; $\sim$15% $\pm$ 14% of *cis* GUVs ($n = 54$) and 53% $\pm$ 11% of *trans* GUVs ($n = 80$) imaged had multiple domains. It is possible that more domains could exist, since domains smaller than the
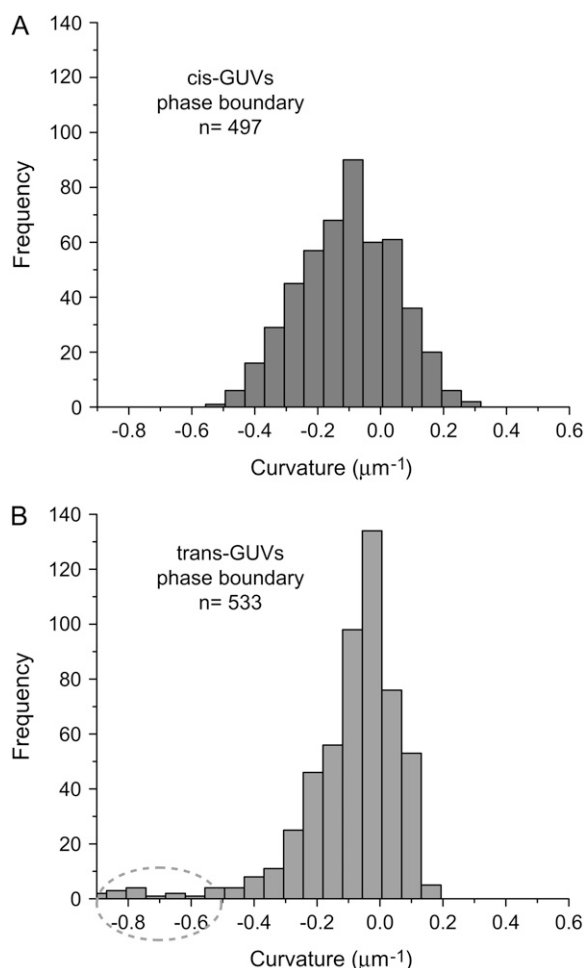
FIGURE 4 Pronounced differences in the distribution of meridional curvatures of *cis* and *trans* GUVs near the phase boundary. Histograms of curvatures (25 bins) of points ± 1 μm on either side of the phase boundary were compiled. The curvature distribution in *trans* GUVs is more skewed toward negative curvature. *Cis* and *trans* GUVs have a similar fraction of negative curvature values at the phase boundary (74% vs. 72%). Despite similarities in the distributions, the mean is different: $\langle C_m \rangle = -0.106 \pm 0.009$ μm^{-1} for *cis* GUVs and $\langle C_m \rangle = -0.092 \pm 0.009$ μm^{-1} for *trans* GUVs, i.e., the *cis* GUVs have a more negative mean meridional curvature near the phase boundary. The features in *trans* GUVs with significantly negative meridional curvatures (<-0.5 μm^{-1}) are indicative of small indentations or invaginations and sharp inward kinks observed in the presence of *trans* DOPC, as seen in Figs. 1 and 2. Upon comparing Figs. 3 and 4 we find that most ($\sim$75%) of the invaginations in the *trans* GUVs are present near the phase boundary. The number of points, *n*, is 497 and 533 for *cis* and *trans* GUVs, respectively.

diffraction limit ($\sim$0.5 μm) could not be resolved. Since multiple domains could potentially coalesce into a single domain given sufficient time, the time between preparation of GUVs and imaging is relevant to the existence or lack of multiple domains in a particular sample. When we compared *cis* and *trans* GUVs imaged within and after 3 days of preparation, more multiple domains were found for *trans* GUVs than for *cis* GUVs. In 0–3 days, 25% of *cis* GUVs and 75% of *trans* GUVs had multiple domains ($n = 20$); after 3

days, 10% of *cis* GUVs and 72% of *trans* GUVs had multiple domains ($n = 28$), where *n* is the total number of vesicles in each of the *cis* and *trans* groups. Thus, the *trans* GUVs, compared to *cis* GUVs, have a larger number of initial multiple domains that persist for a greater length of time.

No difference in mean l_o/l_d area fractions comparing *cis* and *trans* GUVs

Table 3 shows the mean values of area fractions for *cis* and *trans* GUVs. Both sides of axially symmetric equatorial sections of vesicles were analyzed to determine the overall area fraction. Thirty-six GUVs, 18 with *cis* DOPC (*cis* GUVs) and 18 with *trans* DOPC (*trans* GUVs), were analyzed and their results averaged to obtain mean l_o and l_d area fractions. The results indicate that in both cases the l_o area fraction is greater than the l_d area fraction and that the area fractions are similar.

Strong differences in fluorescence intensity distributions of BFL-Spm and Rh-DOPE probes

We use two combinations of fluorescent probes for visualizing membrane domains. The first probe combination consists of Rh-DOPE, which is used as a l_d domain label, and BFL-Spm, which partitions into both domains. Fig. 7 shows probe intensity profiles for BFL-Spm and Rh-DOPE as a function of arc length for *cis* and *trans* GUVs. Rh-DOPE partitions strongly into the l_d phase in both the absence and presence of *trans* DOPC. Table 4 shows the intensity distribution ratios (l_d/l_o values) for the two probe combinations. The values were obtained by averaging traces of at least three GUV equatorial sections. Addition of *trans* DOPC decreases the intensity ratio value for BFL-Spm by $\sim$3-fold compared to *cis* GUVs (Table 4). Rh-DOPE experiences the opposite effect, where its intensity ratio increases $\sim$3.9-fold in the presence of *trans* DOPC (Table 4). Differences in probe brightness within each of the phases are not corrected for.

BFL-Spm and BTR-Spm show similar fluorescence distributions in GUVs

The second probe combination we used was BFL-Spm and BTR-Spm. Fig. 8 shows the probe intensity profiles for the BFL-Spm/BTR-Spm probe combination. Because both probes partition into both phases, discerning the phase boundary is more difficult than for the Rh-DOPE/BFL-Spm pair. However, the phases are still identifiable because the fluorescence intensities (and presumably the partitioning of the dyes) are not identical. The presence of *trans* DOPC weakly decreases the intensity ratio (l_d/l_o) values for both the probes; for both BFL-Spm and BTR-Spm, the value decreases (Table 4).

DISCUSSION

The cell controls various functions by regulating the properties and lateral organization of the plasma membrane (4,9). These properties include parameters such as curvature, line
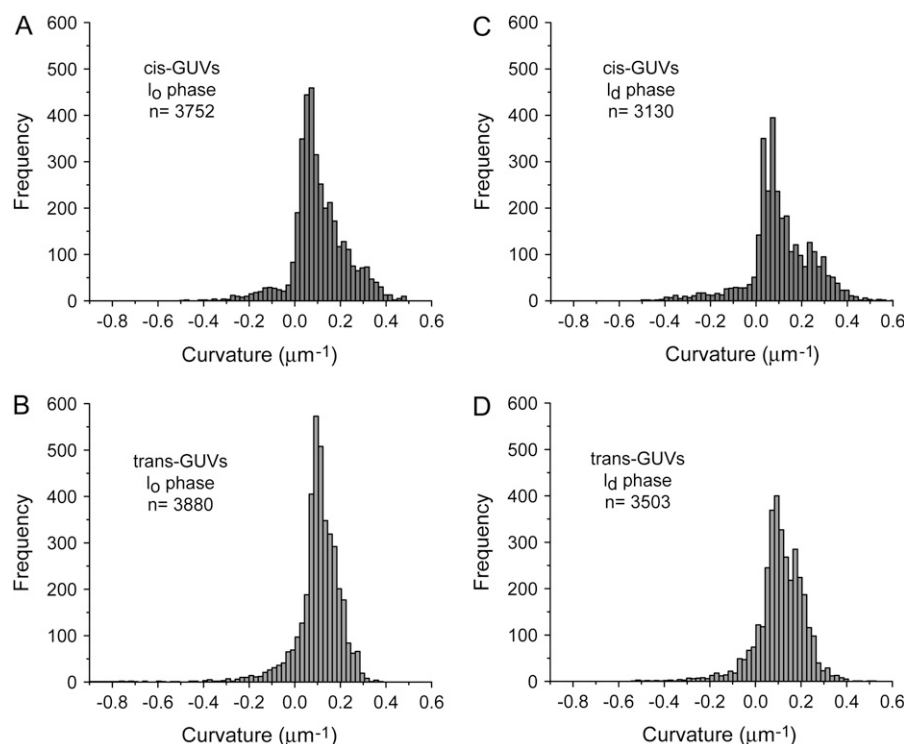
FIGURE 5 Comparison of meridional curvature distributions (75 bins) in the l_o and l_d phases in *cis* and *trans* GUVs. The curvature distribution for *trans* GUVs is similar to that for *cis* GUVs, as determined by the second moment values in the l_o phase ($S = 0.012 \pm 0.002\ \mu m^{-2}$ in *trans* GUVs and $S = 0.014 \pm 0.001\ \mu m^{-2}$ in *cis* GUVs) but different in the l_d phase ($S = 0.012 \pm 0.001\ \mu m^{-2}$ in *trans* GUVs and $S = 0.020 \pm 0.002\ \mu m^{-2}$ in *cis* GUVs). The mean curvature values are similar in the l_o and l_d phases ($\langle C_m \rangle = 0.106 \pm 0.003\ \mu m^{-1}$ in l_o vs. $\langle C_m \rangle = 0.104 \pm 0.004\ \mu m^{-1}$ in l_d) for *cis* GUVs as compared to *trans* GUVs ($\langle C_m \rangle = 0.101 \pm 0.003\ \mu m^{-1}$ in l_o vs. $\langle C_m \rangle = 0.108 \pm 0.003\ \mu m^{-1}$ in l_d).

tension, bending rigidity, and local concentration of various proteins and lipids (8,34–37). Curvature is defined as the inverse of the radius. Negative curvature is defined here as bending inward toward the interior of the GUV (e.g., cytoplasm), and positive curvature as bending outward toward the exterior of the GUV (e.g., extracellular regions).

Clearly there is a significant correlation between membrane curvature and biological function (35). The endoplasmic reticulum and Golgi both feature highly curved membrane structures, which are required for their physiological roles in protein synthesis and intracellular trafficking (38). Phase coexistence in pure lipidic systems also depends
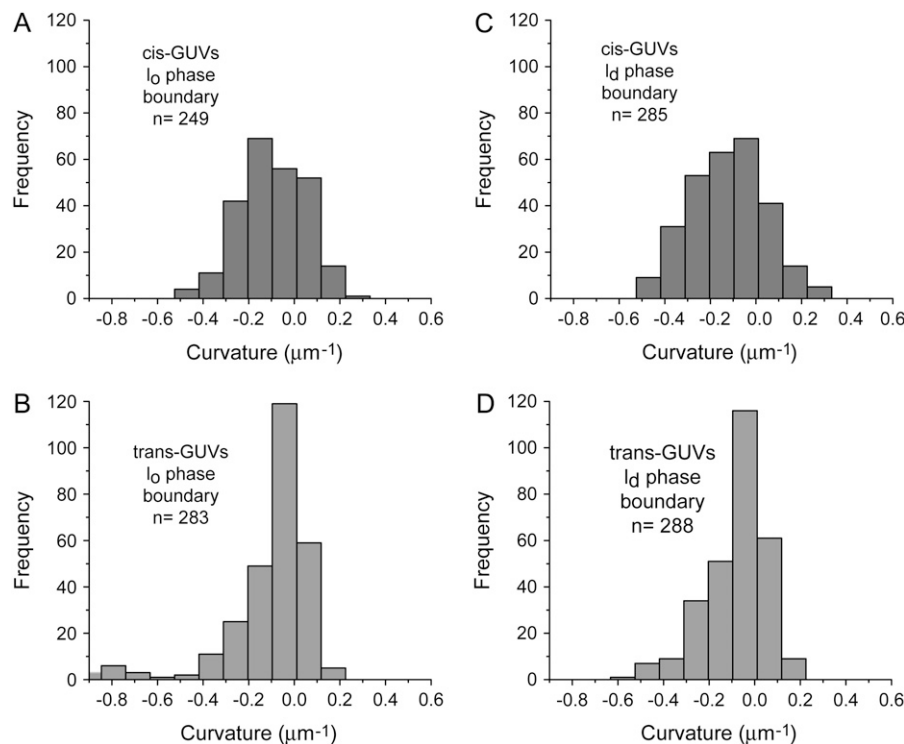

FIGURE 6 Meridional curvature distributions (15 bins) in the l_o and l_d phases near the phase boundary. For *trans* GUVs both the l_o and l_d phase boundary distributions appear to be skewed toward negative curvature values. *Cis* GUVs have a Gaussian-like curvature distribution in both phases. The mean meridional curvature values in the l_o phase for the *cis* and *trans* GUVs are $\langle C_m \rangle = -0.094 \pm 0.013\ \mu m^{-1}$ and $\langle C_m \rangle = -0.103 \pm 0.014\ \mu m^{-1}$, respectively.

TABLE 2 Distribution of meridional curvatures and second moments in the histograms

	Overall		Phase boundary		l_o		l_d		l_o Phase boundary		l_d Phase boundary	
	cis	*trans*	*cis*	*trans*	*cis*	*trans*	*cis*	*trans*	*cis*	*trans*	*cis*	*trans*
Figure No.	3 *A*	3 *B*	4 *A*	4 *B*	5 *A*	5 *B*	5 *C*	5 *D*	6 *A*	6 *B*	6 *C*	6 *D*
Positive (%)	90	90	26	28	91	90	88	89	29	25	22	30
Negative (%)	10	10	74	72	9	10	12	11	71	75	78	70
$\langle C_m \rangle$ (μm^{-1})	0.106	0.105	-0.106	-0.092	0.106	0.101	0.104	0.108	-0.094	-0.103	-0.123	-0.08
	±0.002	±0.002	±0.009	±0.009	±0.003	±0.003	±0.004	±0.003	±0.013	±0.014	±0.014	±0.01
S (μm^{-2})	0.016	0.012	0.023	0.028	0.014	0.012	0.020	0.012	0.021	0.036	0.027	0.019
	±0.001	±0.001	±0.005	±0.006	±0.001	±0.002	±0.002	±0.001	±0.008	±0.012	±0.009	±0.008

Positive and negative percentages of curvature were computed using the number of points (*n*) from Table 1, and indicate the number of points that have positive and negative meridional curvature value, respectively. The mean (meridional) curvature ($\langle C_m \rangle$) and second moment (S) for each category were computed using the histogram corresponding to the figure number indicated. l_o, liquid-ordered; l_d, liquid-disordered.

strongly on membrane lipid composition (23,34,39,40) and strongly couples to local curvature (34), suggesting that many of the same factors determining curvature in model systems may mediate curvature in cell biological systems (36). Curvature can be induced by minimal increases in the number of lipids in one leaflet compared to the other (41), which could certainly result in shape transformations in cell membranes with significant asymmetry. Bacia et al. recently reported that the curvature induced in l_o domains of model membranes is quite sensitive to the type and chemistry of the sterol lipid component (24). Curvature also plays a critical role in membrane fusion and is controlled by the nature of the lipid species present (41,42).

Previous studies of *trans* lipids indicate that, in a similar way to saturated lipids, *trans* lipids have an effect on membrane properties: *trans* DOPC decreases membrane fluidity, permeability, and lateral mobility (43), enhances acyl chain packing (11), interacts strongly with cholesterol (44), and increases cholesterol partition coefficient in bilayers (11). The above results might indicate that *trans* DOPC would have a preference for the l_o phase. We find that *trans* lipids affect membrane morphology, meridional curvature distributions, and intensity ratio values of the fluorescent probes, but not in the way expected for saturated lipids. We categorize the effectsof *trans* lipids on membrane properties as 1), three-dimensional structural effects; and 2), two-dimensional lateral effects.

Three-dimensional structural effects

Structural effects are manifested by changes in vesicle morphology, presence of invaginations or sharp kinks, and alteration of meridional curvature distributions when *trans* DOPC is present. The addition of *trans* DOPC induces unusual

TABLE 3 Mean l_o and l_d area fractions for GUVs without (*cis* DOPC only) and with *trans* DOPC

Type of GUVs	l_o Area fraction	l_d Area fraction
cis GUVs	0.56 ± 0.07	0.44 ± 0.07
trans GUVs	0.57 ± 0.09	0.43 ± 0.09

$N = 18$ for both types of GUVs (*cis* and *trans*).

GUV morphologies that are different from the typical circular and truncated shapes observed in the absence of *trans* lipids. We also find invaginations or indentations in the l_o phase of the membrane in certain GUVs in the presence of *trans* DOPC. These invaginations are reflected in the meridional curvature distributions as well; significantly negative meridional curvatures (<-0.5 μm^{-1}) are observed in *trans* GUVs.

The distribution of meridional curvatures is significantly different despite the fact that the overall fraction of negative curvatures is the same for both *cis* and *trans* GUVs. The curvature distributions are characterized by two parameters, the mean and second moment. The second moment (variance) characterizes the width of the curvature distribution, which is reflective of the bending rigidity. The width of the overall curvature distribution is narrower in the presence of *trans* DOPC; this could be indicative of higher bending rigidity. The overall mean meridional curvature is similar for both types of GUVs. This indicates that although a range of shapes is present, the characteristic size of the shapes is not drastically different in both cases.

Near the phase boundary, the *cis* GUVs have a more negative mean meridional curvature ($\langle C_m \rangle = -0.106$ μm^{-1} for *cis* GUVs and $\langle C_m \rangle = -0.092$ μm^{-1} for *trans* GUVs), though the fraction of negative curvatures is similar for the two populations. This can be explained by the presence of some (strongly) negative curvatures far from the phase boundary in *trans* GUVs. Considering curvature distributions within the l_o phase, near the phase boundary specifically (Fig. 6 *B*), *trans* GUVs have a higher fraction of negative curvatures and a more negative mean curvature. This suggests that the presence of *trans* DOPC may enhance negative curvature within the l_o phase, near the phase boundary.

The width of the l_d meridional curvature distribution is smaller in *trans* GUVs (Fig. 5 *D*) than in *cis* GUVs (Fig. 5 *C*). The width of the curvature distributions could be affected by the range of radii, variety of shapes, and bending rigidity values of the GUV populations. However, the effect on the width due to variation of shapes is reduced, because the shapes analyzed were cylindrically symmetrical, and included primarily spheres and truncated spheres in both *cis* and *trans*
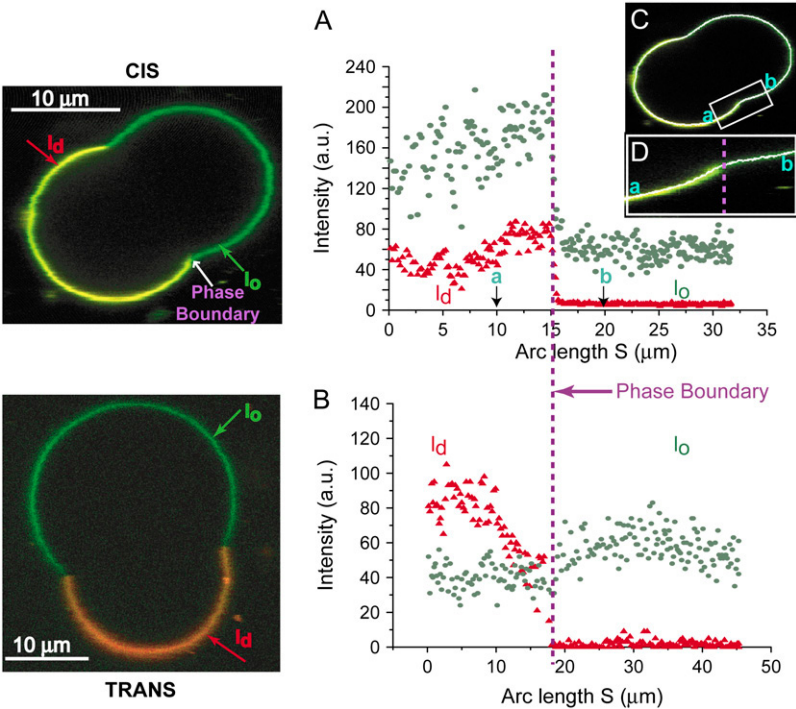
FIGURE 7 Strong differences in fluorescence intensity distributions of BFL-Spm and Rh-DOPE probes. Fluorescence intensities as a function of arc length are plotted for BFL-Spm and Rh-DOPE fluorescent probes in l_o and l_d phases for *cis* (*A*) and *trans* (*B*) GUVs. Rh-DOPE partitions strongly into the l_d phase, whereas the BFL-Spm partitions into both phases. The profiles shown correspond to the GUV equatorial sections depicted on their left but are representative of the general trend. (*C*) Overlay of the shape trace (*white line*) on the GUV shown on the left. (*D*) Zoomed in section of the trace near the phase boundary (not drawn with the same scale as *A*). The shape tracing profile follows the original vesicle very closely. Intensity ratios are computed by first obtaining the average intensity for the probe in each phase on each side of the vesicle and obtaining the l_d/l_o intensity ratio for each probe for that side and thereafter averaging the intensity ratio values on both sides. For *cis*, the total area is ~2001 μm^2, with l_d fraction 0.51 and l_o fraction 0.49; BFL-Spm and Rh-DOPE l_d/l_o intensity ratios are ~2.4 and ~10.3, respectively. For *trans*, the total area is ~4500 μm^2, with l_d fraction 0.30 and l_o fraction 0.70; BFL-Spm and Rh-DOPE l_d/l_o intensity ratios are ~0.75 and ~33, respectively. The values correspond to the GUV sections shown in the figure; mean area fractions and average intensity ratios are tabulated in Tables 3 and 4, respectively.

populations. The major and minor diameter values of a single ellipse that completely encompassed each GUV shape were tabulated to obtain an approximate size range for each GUV. The average minor and major radii were found to be 8.7 ± 5.6 μm and 12.5 ± 8.4 μm for *cis* GUVs; *trans* GUVs had minor and major radii values of 7.8 ± 2.3 μm and 10.7 ± 2.7 μm, respectively. This would correspond to curvature value ranges from 0.115 to 0.08 μm^{-1} in *cis* GUVs and 0.128 to 0.093 μm^{-1} in *trans* GUVs; the curvature span is 0.035 μm^{-1} in both cases. Since the average radii and curvature spans are similar, differences in the radii of vesicles between the *cis* and *trans* populations cannot account for the differences in curvature distributions. Therefore, it is plausible (although not proven directly) that the variation in the width of the distributions is reflective of the bending rigidity differences between *cis* and *trans* GUVs. The width of the l_d curvature distribution (Fig. 5 *C*) is greater than that seen in the l_o phase (Fig. 5 *A*) in *cis* GUVs, possibly reflecting lower bending rigidity in the l_d phase. The addition of *trans* DOPC alters the

width of the curvature distribution significantly (Table 2, *bottom row*) in the l_d phase (Fig. 5 *D*) when compared to the *cis* population (Fig. 5 *C*); this narrowing could be due to the partitioning of *trans* DOPC into the l_d phase, thereby rendering it more rigid.

The meridional curvature distributions are also reflective of changes in GUV morphology and the presence of invaginations. Since membrane curvature is influenced by the lipid environment and domain composition (34), the structural changes observed in the presence of *trans* DOPC in cells may result in changes in membrane function or organization. Since rafts and raft-mediated proteins are affected by changes in membrane composition (2,45), curvature alterations may perturb the distribution and therefore the function of raft-associated proteins such as the SR-B1 receptor (46). In the context of heart disease, *trans* lipids could consequently lead to alteration of high-density lipoprotein metabolism. Also, curvature is coupled to line tension, which plays a key role in raft formation (34,47).

Two-dimensional lateral effects

Lateral effects are characterized by the presence or absence of multiple domains, l_o/l_d area fractions, and the distribution of fluorescent probes as determined by their l_d/l_o intensity ratios.

Domain coalescence

A greater number of samples exhibit multiple domains (more than two) in the presence of *trans* lipids than the control. The

TABLE 4 Intensity ratio values for fluorescent probes BFL-Spm, Rh-DOPE, and BTR-Spm in *cis* and *trans* GUVs

Intensity ratio	BFL-Spm/Rh-DOPE		BFL-Spm/BTR-Spm	
	BFL-Spm l_d/l_o	Rh-DOPE l_d/l_o	BFL-Spm l_d/l_o	BTR-Spm l_d/l_o
cis GUVs	2.46 ± 0.24	9.45 ± 1.10	1.27 ± 0.25	1.79 ± 0.25
trans GUVs	0.80 ± 0.08	36.78 ± 9.09	1.07 ± 0.20	1.53 ± 0.26

The intensity ratios are computed as the ratios of the average fluorescent intensities of the probe in the liquid-disordered (l_d) and liquid-ordered (l_o) phase for each probe. The values were obtained by averaging at least three GUV sections.
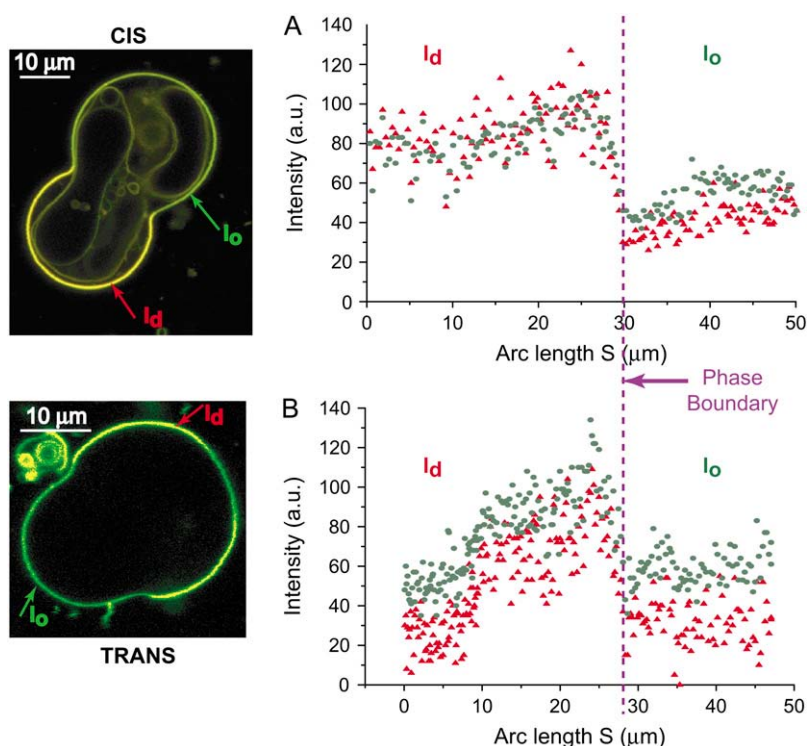
FIGURE 8   BFL-Spm and BTR-Spm show similar fluorescence distributions in GUVs. BFL-Spm and BTR-Spm partition into both the phases and show similar fluorescence intensity profiles. The profiles shown in the figure mirror the general trend observed in GUVs with the BFL-Spm/ BTR-Spm probe combination. For *cis*, the total area is ~ 7655 μm^2, with l_d fraction 0.43 and l_o fraction 0.57; BFL-Spm and BTR-Spm l_d/l_o intensity ratios are ~ 1.61 and ~ 2.16, respectively. For *trans*, the total area is ~ 4535 μm^2, with l_d fraction 0.67 and l_o fraction 0.33; BFL-Spm and BTR-Spm l_d/l_o intensity ratios are ~ 1.28 and ~ 1.74, respectively. The above values correspond to the GUV sections shown in the figure.

presence of multiple domains could not be accounted for by the time elapsed between sample preparation and imaging. For the same time elapsed between preparation and imaging, a greater number of *trans* lipid samples had multiple domains than their *cis* counterparts. As is suggested by the narrower distribution of curvatures, increased membrane bending modulus in the presence of *trans* lipids could inhibit close approach of curved domains, decreasing the coalescence rate. The presence of a larger fraction of vesicles with multiple domains in *trans* GUVs than in *cis* GUVs may be due to either a reduced domain coalescence rate and/or a greater initial number of domains in the presence of *trans* DOPC. Rafts are l_o domains in the membrane with distinct compositions; they are formed due to lipid-lipid immiscibility giving rise to lateral inhomogeneities (7). Since domain coalescence is involved in certain cell functions such as signal transduction (9), inhibition of domain coalescence is one way that *trans* lipids could perturb cell function.

l_o/l_d area fractions and probe partitioning

Since *trans* DOPC does not affect the relative area fractions of l_o and l_d phases, we conclude that it does not act like the saturated lipid egg sphingomyelin. The question that consequently arises is into which phase(s) *trans* DOPC partitions. If *trans* DOPC were to act similarly to a saturated lipid (such as egg sphingomyelin), one would expect it to partition strongly into the l_o phase and result in an increase in l_o area fraction in *trans* GUVs compared to *cis* GUVs. However, the observed relative l_o/l_d area fractions are similar for both, indicating that *trans* DOPC probably partitions into both

phases. Moreover, both phases experience changes in curvature distributions when *trans* DOPC is present, further strengthening the idea that *trans* DOPC could be present in both.

Trans lipids decrease the l_d/l_o intensity ratio values of the fluorescent probes BFL-Spm and BTR-Spm and increase the value for Rh-DOPE. Rh-DOPE partitions strongly into the l_d phase, whereas BFL-Spm and BTR-Spm partition into both. The intensity of a probe in a particular phase is proportional to the product of the concentration and the brightness. The brightness is in turn influenced by the lipid environment that the probe experiences. *Trans* lipids either alter partitioning of the probes studied here, change the lipid environment in such a way that the brightness of the probes is affected, or both. *Trans* DOPC could perturb cell function by altering membrane parameters, since protein function in membranes is influenced by membrane properties such as the composition and local order in the lipid environment (37).

Potential applications of BFL-Spm, BFL-TR, and Rh-DOPE probe combinations

For imaging applications where determination of the location of the phase boundary is crucial, the BFL-Spm/Rh-DOPE combination is advantageous due to the strong partitioning behavior of Rh-DOPE, which makes identification of the l_d phase straightforward. We observe similar results using two different probe combinations, indicating that in comparing vesicles with and without *trans* lipids, the choice of probes used does not strongly alter the observed differences. On the

other hand, one can also use the minimum possible probe concentration to avoid perturbation of the system by the probes. FCS measurements can be carried out at extremely low probe concentrations (<0.1 molecules/μm^2), followed by much higher concentrations (>100 molecules/μm^2) to test whether membrane properties change over a wide range of probe concentrations. Determination of useful probe combinations for such measurements is therefore a useful first step. The dye pair BFL-Spm and BTR-Spm has potential for applications where double-labeling of the same domain with two probes is desirable (e.g., energy transfer or fluorescence cross-correlation spectroscopy).

SUMMARY

Trans unsaturated lipids mediate membrane properties differently than their *cis* counterparts. *Trans* lipids induce unusual vesicle morphologies that differ from the typical circular and truncated shapes observed in their absence, and they have an especially strong effect on membrane curvature in the l$_o$ phase near the phase boundary. There, *trans* lipids induce significantly negative ($<-0.5~\mu$m^{-1}) meridional curvatures, and occasional strongly curved membrane invaginations. Compared to *cis*, greater numbers of multiple domains are observed in the presence of *trans* DOPC, potentially due to reduced domain coalescence rates. Fluorescent probe distributions reveal that the l$_d$/l$_o$ intensity ratio values are also altered in the presence of *trans* DOPC. These results could be important for understanding how *trans* lipids affect cellular functions that are controlled by curvature, such as fusion, fission, and endocytosis. Future experiments could investigate higher mole fractions of *trans* lipids. It has been shown that *trans* isomers of the polyunsaturated *trans* fat linoelaidic acid are associated with a greater risk of cardiac arrest than *trans* isomers (e.g., elaidic acid) of the monounsaturated *trans* fat oleic acid (17), suggesting that they possess different biophysical properties. Experiments incorporating and comparing different types of *trans* lipids would be highly beneficial in unraveling the connection between *trans* fats and cellular function.

REFERENCES

1. Anderson, R. G. W., and K. Jacobson. 2002. Cell biology. A role for lipid shells in targeting proteins to caveolae, rafts, and other lipid domains. *Science*. 296:1821–1825.

2. Brown, D. A., and E. London. 1998. Functions of lipid rafts in biological membranes. *Annu. Rev. Cell Dev. Biol.* 14:111–136.

3. Simons, K., and D. Toomre. 2000. Lipid rafts and signal transduction. *Nat. Rev. Mol. Cell Biol.* 1:31–39.

4. Mukherjee, S., and F. R. Maxfield. 2004. Membrane domains. *Annu. Rev. Cell Dev. Biol.* 20:839–866.

5. Brown, D. A., and E. London. 2000. Structure and function of sphingolipid- and cholesterol-rich membrane rafts. *J. Biol. Chem.* 275:17221–17224.

6. Simons, K., and E. Ikonen. 1997. Functional rafts in cell membranes. *Nature*. 387:569–572.

7. Rajendran, L., and K. Simons. 2005. Lipid rafts and membrane dynamics. *J. Cell Sci.* 118:1099–1102.

8. Baumgart, T., S. Das, W. W. Webb, and J. T. Jenkins. 2005. Membrane elasticity in giant vesicles with fluid phase coexistence. *Biophys. J.* 89:1067–1080.

9. Simons, K., and R. Ehehalt. 2002. Cholesterol, lipid rafts, and disease. *J. Clin. Invest.* 110:597–603.

10. Manes, S., G. del Real, and C. Martinez-A. 2003. Pathogens: raft hijackers. *Nat. Rev. Immunol.* 3:557–568.

11. Niu, S. L., D. C. Mitchell, and B. J. Litman. 2005. *Trans* fatty acid derived phospholipids show increased membrane cholesterol and reduced receptor activation as compared to their *cis* analogs. *Biochemistry*. 44:4458–4465.

12. Ascherio, A., M. B. Katan, P. L. Zock, M. J. Stampfer, and W. C. Willett. 1999. *Trans* fatty acids and coronary heart disease. *N. Engl. J. Med.* 340:1994–1998.

13. Zapolska-Downar, D., A. Kosmider, and M. Naruszewicz. 2005. *Trans* fatty acids induce apoptosis in human endothelial cells. *J. Physiol. Pharmacol.* 56:611–625.

14. Baylin, A., E. K. Kabagambe, A. Ascherio, D. Spiegelman, and H. Campos. 2003. High 18:2 *trans*-fatty acids in adipose tissue are associated with increased risk of nonfatal acute myocardial infarction in Costa Rican adults. *J. Nutr.* 133:1186–1191.

15. Allison, D. B., S. K. Egan, L. M. Barraj, C. Caughman, M. Infante, and J. T. Heimbach. 1999. Estimated intakes of *trans* fatty and other fatty acids in the US population. *J. Am. Diet. Assoc.* 99:166–174.

16. Clifton, P. M., J. B. Keogh, and M. Noakes. 2004. *Trans* fatty acids in adipose tissue and the food supply are associated with myocardial infarction. *J. Nutr.* 134:874–879.

17. Lemaitre, R. N., I. B. King, T. E. Raghunathan, R. M. Pearce, S. Weinmann, R. H. Knopp, M. K. Copass, L. A. Cobb, and D. S. Siscovick. 2002. Cell membrane *trans*-fatty acids and the risk of primary cardiac arrest. *Circulation*. 105:697–701.

18. Semma, M. 2002. *Trans* fatty acids: Properties, benefits and risks. *J. Health Sci.* 48:7–13.

19. Kummerow, F. A., Q. Zhou, M. M. Mahfouz, M. R. Smiricky, C. M. Grieshop, and D. J. Schaeffer. 2004. *Trans* fatty acids in hydrogenated fat inhibited the synthesis of the polyunsaturated fatty acids in the phospholipid of arterial cells. *Life Sci.* 74:2707–2723.

20. Kummerow, F. A., Q. Zhou, and M. M. Mahfouz. 1999. Effect of *trans* fatty acids on calcium influx into human arterial endothelial cells. *Am. J. Clin. Nutr.* 70:832–838.

21. Dietrich, C., L. A. Bagatolli, Z. N. Volovyk, N. L. Thompson, M. Levi, K. Jacobson, and E. Gratton. 2001. Lipid rafts reconstituted in model membranes. *Biophys. J.* 80:1417–1428.

22. Bagatolli, L. A., and E. Gratton. 1999. Two-photon fluorescence microscopy observation of shape changes at the phase transition in phospholipid giant unilamellar vesicles. *Biophys. J.* 77:2090–2101.

23. Veatch, S. L., and S. L. Keller. 2003. A closer look at the canonical 'raft mixture' in model membrane studies. *Biophys. J.* 84:725–726.

24. Bacia, K., P. Schwille, and T. Kurzchalia. 2005. Sterol structure determines the separation of phases and the curvature of the liquid-ordered phase in model membranes. *Proc. Natl. Acad. Sci. USA*. 102:3272–3277.

25. Veatch, S. L., and S. L. Keller. 2003. Separation of liquid phases in giant vesicles of ternary mixtures of phospholipids and cholesterol. *Biophys. J.* 85:3074–3083.

26. Stachowska, E., B. Dolegowska, D. Chlubek, T. Wesolowska, K. Ciechanowski, P. Gutowski, H. Szumilowicz, and R. Turowski. 2004. Dietary *trans* fatty acids and composition of human atheromatous plaques. *Eur. J. Nutr.* 43:313–318.

27. Mathivet, L., S. Cribier, and P. F. Devaux. 1996. Shape change and physical properties of giant phospholipid vesicles prepared in the presence of an AC electric field. *Biophys. J.* 70:1112–1121.

28. Veatch, S. L., and S. L. Keller. 2005. Seeing spots: complex phase behavior in simple membranes. *Biochim. Biophys. Acta.* 1746:172–185.

29. Hess, S. T., M. V. Gudheti, M. Mlodzianoski, and T. Baumgart. 2007. Shape analysis of giant vesicles with fluid phase coexistence by laser scanning microscopy to determine curvature, bending elasticity, and line tension. *In* Methods in Membrane Lipids. A. Dopico, editor. Humana Press, Totowa, NJ. In press.

30. de Almeida, R. F. M., L. M. S. Loura, A. Fedorov, and M. Prieto. 2005. Lipid rafts have different sizes depending on membrane composition: a time-resolved fluorescence resonance energy transfer study. *J. Mol. Biol.* 346:1109–1120.

31. Samsonov, A. V., I. Mihalyov, and F. S. Cohen. 2001. Characterization of cholesterol-sphingomyelin domains and their dynamics in bilayer membranes. *Biophys. J.* 81:1486–1500.

32. Ayuyan, A. G., and F. S. Cohen. 2006. Lipid peroxides promote large rafts: effects of excitation of probes in fluorescence microscopy and electrochemical reactions during vesicle formation. *Biophys. J.* 91:2172–2183.

33. Glascott, P. A., M. Tsyganskaya, E. Gilfor, M. A. Zern, and J. L. Farber. 1996. The antioxidant function of the physiological content of vitamin C. *Mol. Pharmacol.* 50:994–999.

34. Baumgart, T., S. T. Hess, and W. W. Webb. 2003. Imaging coexisting fluid domains in biomembrane models coupling curvature and line tension. *Nature.* 425:821–824.

35. McMahon, H. T., and J. L. Gallop. 2005. Membrane curvature and mechanisms of dynamic cell membrane remodelling. *Nature.* 438:590–596.

36. Zimmerberg, J., and M. M. Kozlov. 2006. How proteins produce cellular membrane curvature. *Nat. Rev. Mol. Cell Biol.* 7:9–19.

37. McIntosh, T. J., and S. A. Simon. 2006. Roles of bilayer material properties in function and distribution of membrane proteins. *Annu. Rev. Biophys. Biomolec. Struct.* 35:177–198.

38. Alberts, B. 2002. Molecular biology of the cell. Garland Science, New York.

39. Korlach, J., P. Schwille, W. W. Webb, and G. W. Feigenson. 1999. Characterization of lipid bilayer phases by confocal microscopy and fluorescence correlation spectroscopy. *Proc. Natl. Acad. Sci. USA.* 96:8461–8466.

40. Veatch, S. L., and S. L. Keller. 2002. Organization in lipid membranes containing cholesterol. *Phys. Rev. Lett.* 89:268101(1)–268101(4).

41. van Meer, G., and H. Sprong. 2004. Membrane lipids and vesicular traffic. *Curr. Opin. Cell Biol.* 16:373–378.

42. Chernomordik, L. V., and M. M. Kozlov. 2003. Protein-lipid interplay in fusion and fission of biological membranes. *Annu. Rev. Biochem.* 72:175–207.

43. Roach, C., S. E. Feller, J. A. Ward, S. R. Shaikh, M. Zerouga, and W. Stillwell. 2004. Comparison of *cis* and *trans* fatty acid containing phosphatidylcholines on membrane properties. *Biochemistry.* 43:6344–6351.

44. Jing, B., N. Tokutake, D. H. McCullough, and S. L. Regen. 2004. A quantitative assessment of the influence of permanent kinks on the mixing behavior of phospholipids in cholesterol-rich bilayers. *J. Am. Chem. Soc.* 126:15344–15345.

45. Holowka, D., J. A. Gosse, A. T. Hammond, X. M. Han, P. Sengupta, N. L. Smith, A. Wagenknecht-Wiesner, M. Wu, R. M. Young, and B. Baird. 2005. Lipid segregation and IgE receptor signaling: a decade of progress. *Biochim. Biophys. Acta.* 1746:252–259.

46. Frank, P. G., S. E. Woodman, D. S. Park, and M. P. Lisanti. 2003. Caveolin, caveolae, and endothelial cell function. *Arterioscler. Thromb. Vasc. Biol.* 23:1161–1168.

47. Kuzmin, P. I., S. A. Akimov, Y. A. Chizmadzhev, J. Zimmerberg, and F. S. Cohen. 2005. Line tension and interaction energies of membrane rafts calculated from lipid splay and tilt. *Biophys. J.* 88:1120–1133.